

# Tempering and Precipitation Behavior of 7 Pct Cr-0.1 Pct V-0.06 Pct Nb-0.08 Pct N Steel

M. TAMURA, M. NAKAMURA, K. SHINOZUKA, and H. ESAKA

In order to clarify the tempering and precipitation behavior of carbon-free and nitrogen-bearing high-chromium martensitic steel, an experimental steel was newly designed and examined precisely. Tempering was performed at 650 °C to 800 °C for a maximum of 1000 hours. In addition to the general trend of recovery, discontinuous changes in hardness and bulk X-ray properties were observed during the tests. Fine particles of the NaCl type (MX) and coarse, platelike Cr<sub>2</sub>N particles containing small amounts of V and Nb were observed. The average chemical composition of MX changed from (Cr<sub>0.65</sub>V<sub>0.25</sub>Nb<sub>0.1</sub>)N to (Cr<sub>0.35</sub>V<sub>0.45</sub>Nb<sub>0.2</sub>)N, with the progress of tempering. Even after tempering at 750 °C for 1000 hours, the chemical composition of the MX was distributed widely around the average value. The size of the MX nitride gradually increased from 20 to 60 nm in 1000 hours at 750 °C, and the apparent time exponent was roughly 0.25. When the discontinuous changes in hardness were observed, the amount of both the MX and the Cr<sub>2</sub>N and the composition of the MX changed, discontinuously. This suggested that, accompanying the formation of subgrains during tempering, the particles precipitated on the boundaries repeatedly dissolved into the matrix, followed by reprecipitation.

DOI: 10.1007/s11661-008-9486-5

© The Minerals, Metals & Materials Society and ASM International 2008

## I. INTRODUCTION

FROM the historical point of view, it is well known that a very small amount of nitrogen and molybdenum in solid solution remarkably increases the creep-rupture strength of carbon steel;<sup>[1]</sup> in low- and high-chromium heat-resistant steel, however, nitrogen formed AlN or CrN, and, as a consequence, nitrogen had not been considered as taking an active role and had not been intentionally added to heat-resistant steel for a long time. About a quarter century ago, when a modified 9Cr steel was invented,<sup>[2]</sup> 0.04 pct of nitrogen was added, along with a small amount of strong carbo-nitride formers of V and Nb. Since that time, it has been well known that finely dispersed precipitates retard the recovery of high-chromium martensitic heat-resistant steel<sup>[3]</sup> and that MX carbo-nitride (in which M means metallic element and X is carbon and nitrogen), rather than MX carbide, is important for improving the creep-rupture strength of steel.<sup>[4]</sup>

Chromium carbide of M<sub>23</sub>C<sub>6</sub> is popular, but grew easily, hence, the size of these particles was somewhat larger than that of the MX particles in general. The growth of M<sub>23</sub>C<sub>6</sub> particles precipitated on lath or block boundaries caused the migration of grain boundaries and, therefore, shortened the time to the onset of acceleration creep.<sup>[5,6]</sup> The size of the MX was about 15

to 30 nm in the as-tempered state,<sup>[7,8]</sup> but the size increased up to about 70 nm by heating at 650 °C for approximately 10,000 hours.<sup>[7]</sup> Therefore, in order to control the distribution of fine particles, many researchers have focused on the precipitation behavior of M<sub>23</sub>C<sub>6</sub>,<sup>[9,10]</sup> MX particles,<sup>[7,8,11]</sup> and Z phase,<sup>[12]</sup> which was formed at the expense of the MX particles in martensitic steel, and have intended to optimize the chemical composition and heat treatment of martensitic heat-resistant steel.

In line with these considerations, Taneike *et al.*<sup>[13,14]</sup> have developed a steel with 0.003 pct C-9 pct Cr-3 pct W-3 pct Co-0.2 pct V-0.06 pct Nb-0.05 pct N. This steel precipitated only MX nitride with a small amount of Laves phase, but did not precipitate M<sub>23</sub>C<sub>6</sub>, Cr<sub>2</sub>N, and Z phase within the test conditions. The shape of the MX in the newly developed steel was cubic, with an initial size of 5 to 10 nm. Sawada *et al.*<sup>[15]</sup> reported that Z phase was formed at the expense of the strengthening particles of the MX nitride after creep exposure for about 10,000 hours in the developed steel; however, the amount of Z phase was not reported. The steel was strengthened by MX-type nitride rather than MX-type carbo-nitride and has shown the highest rupture strength at 650 °C among martensitic steels produced by melting practice.<sup>[13]</sup>

Concerning the stability of the MX particles in martensitic steel, Tamura *et al.*<sup>[16]</sup> reported an unfamiliar phenomenon: the stable VN particles, which were precipitated during tempering, once dissolved into the matrix and finally precipitated again. A similar phenomenon was confirmed in a steel that precipitated TaC.<sup>[17]</sup> It was also reported that discontinuous changes in both the hardness and integral breadth of an X-ray diffraction (XRD) peak of the ferrite matrix were

M. TAMURA and H. ESAKA, Professors, and K. SHINOZUKA, Research Associate, are with the M&E Department, National Defense Academy, Yokosuka-shi, 2398686, Japan. Contact e-mail: hesaka@nda.ac.jp M. NAKAMURA, formerly with the Graduate School, National Defense Academy, is with Japan Ground Self Defense Force, Shizuoka, Japan.

Manuscript submitted April 1, 2007.

Article published online March 28, 2008

observed; these changes accompanied the dissolution of VN and TaC particles. Using an atom probe field ion microscope, Jayaram and Klueh<sup>[11]</sup> showed that nearly all of the tantalum was in the solid solution of the ferrite matrix of the normalized and tempered 7Cr2WVTa steel. However, the solubility equations for TaC<sup>[18,19]</sup> surely showed that TaC should precipitate in the normalized state of the steel. This indicated that the TaC particles formed in the normalized state should dissolve during tempering. Moreover, several reports have been found in the literature that the MX particles precipitated during normalizing were dissolved temporarily into the matrix during tempering and that, finally, the fine MX particles precipitated again.<sup>[20,21]</sup> Therefore, it has been well established that MX particles precipitated in martensite are fine; it was also found that, in some cases, MX particles that precipitated stably in ferrite or austenite could possibly dissolve and precipitate again.

In order to estimate the long-term creep strength of carbon-free, nitrogen-bearing, high-strength steels, it is very important to characterize the MX nitride in the steels and clarify its stability. However, the long-term stability and character of MX nitride during creep have not been investigated sufficiently. On the other hand, it is also well known that the long-term creep behavior of ferritic steel is related to the tempering characteristics of the steel.<sup>[3]</sup>

Therefore, a nitrogen-bearing steel without carbon was redesigned based on the modified 9Cr steel and was tempered in a wide range of both temperatures and time; then, precipitation behavior during tempering of the experimental steel was studied systematically. The carbon was replaced by nitrogen; then, in order to avoid the formation of  $\delta$  ferrite and Cr<sub>2</sub>N, the content of the Cr, Si, Mo, and V was controlled using a thermodynamic data calculation system.<sup>[22]</sup> However, Cr<sub>2</sub>N particles were also formed in the experimental steel. A phase of Cr<sub>2</sub>N was reported to increase the coarsening rate of MX nitride in nitrogen-bearing steel<sup>[15]</sup> and, therefore, we investigated both MX and Cr<sub>2</sub>N.

## II. EXPERIMENTAL PROCEDURE

The chemical composition of the experimental steel NBN2 is shown in Table I. The steel was vacuum-induction cast in the form of a 50-kg ingot; the ingot was heated at 1250 °C and hot-rolled to a 12-mm thickness. The hot-rolled plate was heated at 1250 °C for 2 hours and air cooled. Small coupons cut from the normalized plate were rapidly heated in a furnace preheated to a temperature between 650 °C and 800 °C and soaked for a maximum of 1000 hours.

The microstructures of the tempered specimens were examined using an optical microscope and a scanning

electron microscope; the Vickers hardness was measured under a 10-kg load.

A longitudinal cross section was cut using a 100-grit aluminum cutter and ground by SiC papers, the finest grit of which was 800. After the mechanical grinding, 0.2 mm from the surface was removed electrically using a 10 pct acetyl acetone-1 pct tetramethyl ammonium chloride methanol electrolyte solution (10 pct AA solution). The rolling direction was set perpendicular to the X-ray, and (110), (200), (211), (220), and (310) diffraction peaks of the matrix were obtained using a Cu K<sub>α</sub> line. The integral breadth for each peak of the matrix was measured; the apparent lattice strain,  $\eta$ , and the apparent size of the crystalline particle,  $\varepsilon$ , were analyzed from the integral breadths using the Hall's relation:<sup>[23]</sup>

$$\frac{\beta \cos \theta}{\lambda} = \frac{1}{\varepsilon} + \eta \frac{\sin \theta}{\lambda} \quad [1]$$

where  $\beta$  is the integral breadth,  $\theta$  is the Bragg angle, and  $\lambda$  is the X-ray wavelength. In the analysis, the standard Si powder made by the National Institute of Standards and Technology (Gaithersburg, MD) was used as a reference material.

In order to check the nitrogen pickup during tempering, a 2-mm layer was mechanically removed from all surfaces of a tempered specimen; the content of nitrogen was then measured. The results are shown in Figure 1; the figure shows that there is no evidence of nitrogen pickup during long-term tempering in air at 750 °C. After removing the surface layer, a specimen was electrolyzed in a 10 pct AA solution; the residue was separated using a filter with 0.1- $\mu$ m pores (Track-Etched Membrane filter by Whatman, Japan KK, Tokyo, Japan) placed on a filter base connected to a water

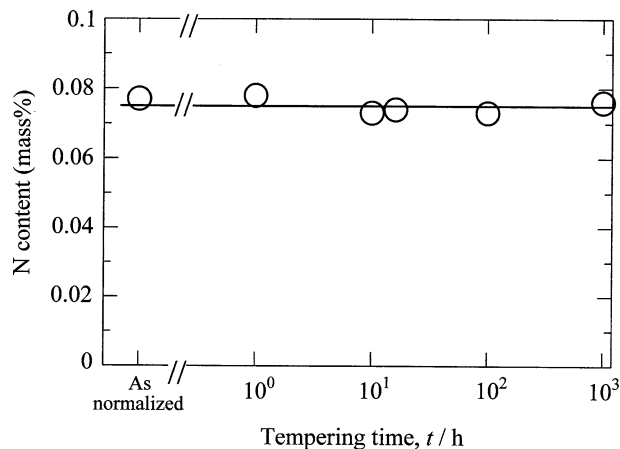


Fig. 1—Nitrogen content of specimens tempered at 750 °C.

Table I. Chemical Composition of Experimental Steel; Balance is Fe (Mass Percent)

Material	C	Si	Mn	P	S	Cr	Mo	V	Nb	Al	N
NBN2	0.003	0.16	0.52	0.002	0.002	7.03	0.1	0.1	0.063	0.02	0.077

aspirator. The extracted residue, together with a filter, was examined using an X-ray diffractometer. The measured integral breadth was corrected using the standard Si powder; the apparent sizes of the precipitates were calculated using the Scherrer's relation, on the assumption that the Scherrer's constant,  $K$ , was unity.<sup>[24]</sup> The chemical composition of the residue was determined using inductively coupled plasma-atomic emission spectroscopy (ICP-AES).

Extracted carbon replicas were observed using a field emission transmission electron microscope (Hitachi, Ltd., Tokyo, Japan) operating at 200 kV. The chemical compositions of typical particles on the replicas were analyzed using energy dispersive spectroscopy (EDS) (Topcon Technohouse Co., Tokyo, Japan).

### III. EXPERIMENTAL RESULTS

#### A. Bulk Properties

##### 1. Normalized state

The microstructure of the normalized specimen at 1250 °C was 100 pct martensite, and  $\delta$  ferrite was not found using optical microscopy (OM). Though MX phase was not detected in the extracted residue using XRD, few Nb-rich particles were found on boundaries using scanning electron microscopy (SEM). The chemical composition of the metallic elements of the niobium-rich compound was measured as 84.3 pct Nb-8 pct V-4 pct Cr-3 pct Mo-0.7 pct Fe in atomic percent, using extraction carbon replicas. The average particle size was 62 nm and the aspect ratio was 1.3. These particles might be undissolved Nb-rich MX phase.

##### 2. Tempered state

*a. Hardness.* Figure 2 shows the isothermal tempering curves of the hardness of the NBN2, for temperatures shown in the figure. The hardness, in general, decreased linearly with the logarithm of tempering time. However, small and discontinuous changes on a hardness curve were observed for the NBN2 between 4 and 300 hours, depending on the tempering temperature, while a peak height was largest at 650 °C, and small and discontinuous changes were observed for 12.5, 45, and 300 hours at 750 °C. In Figure 2, the maximum and minimum values among the 10 measured values are connected by a bar, while the bars show only typical tempering conditions, for simplicity. This showed that most data ranged within the size of each symbol. The enlarged subfigure in Figure 2 shows all measured values for 750 °C around 12.5 hours. It was found from the enlarged figure in Figure 2 that the crest and trough in a hardness curve occurred near the discontinuous change at 12.5 hours. At 45 and 300 hours, a discontinuous change in hardness was not as clear, but the slope of the hardness curve changed after these tempering times. Therefore, the discontinuous changes observed at these three times in the hardness curve were thought to be significant. These three times, 12.5, 45, and 300 hours, will be referred to in subsequent figures and indicated by

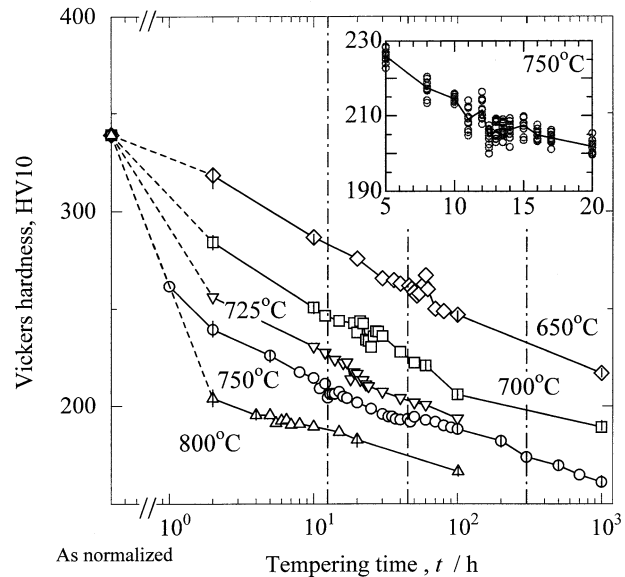


Fig. 2—Isothermal tempering curves of Vickers hardness. Vertical bars at symbols denote a range of maximum and minimum. Vertical dash-dotted lines denote times for occurrence of crest and trough in hardness curve at 750 °C, *i.e.*, 12.5, 45, and 300 h. Similar vertical dash-dotted lines are drawn in subsequent figures, but explanation is omitted, hereafter.

vertical dash-dotted lines. These discontinuous changes in a tempering curve of hardness had not been explicitly noticed earlier.<sup>[25]</sup> However, similar unfamiliar changes in hardness during tempering, as shown in Figure 2, were recently reported.<sup>[16,17,26]</sup>

*b. Microstructure by OM and SEM.* Carbide precipitated on the grain boundaries from the early stages of tempering. A lath martensite-like structure surrounded by precipitates seemed to grow with increasing tempering time, which might relate to a previous observation of the increase in the width of martensite lath caused by creep damage.<sup>[9]</sup> However, the characteristic changes corresponding to the discontinuous changes in hardness shown in Figure 2 were not found.

*c. XRD of bulk specimens.* Five matrix peaks, (110), (200), (211), (220), and (310), of the tempered specimens at 750 °C were obtained using XRD. Specific intensity,  $I_{(hkl)}/I_{(110)}$ , is shown in Figure 3 as a function of tempering time, where  $I_{(hkl)}$  is the integrated intensity for an  $(hkl)$  peak. The figure shows that the specific intensity largely varied within a short interval and, especially, that the specific intensity fluctuated largely at the time of the occurrence of the discontinuous changes in a hardness curve, as shown in Figure 2, except for the specific intensity of  $I_{(220)}/I_{(110)}$ . The specific intensity of  $I_{(220)}/I_{(110)}$  should logically remain constant within the experimental error, because a plane of (220) is parallel to (110). Except for a (220) plane, the specific intensity varied largely during tempering and was also reported for a 9 pct Cr-1 pct Mo-0.2 pct V steel; when these results were combined with the results of the inverse pole figures, the conclusion was reached that the rotation of

the preferred orientation occurred discontinuously when the crest and trough were observed within a short period, in a specific intensity-*vs*-tempering time curve.<sup>[26]</sup> Therefore, Figure 3 implies that the drastic rotation of the preferred orientation should occur repeatedly between 12.5 and 300 hours at 750 °C, although we have not yet constructed inverse pole figures for the experimental steel.

The integral breadths for each diffraction peak of the matrix were also measured and were converted to the apparent lattice strain,  $\eta$ , and the apparent crystalline particle size,  $\varepsilon$ , using Eq. [1]; the results are shown in Figure 4. The apparent lattice strain of the normalized state was released due to the progress of tempering and, contrary to expectations, the apparent crystalline particle size kept constant with the increase in tempering time, except near 12.5 and 45 hours. The general trend shown in Figure 4 did not contradict well-established metallurgical knowledge. However, it was also found in Figure 4 that both the apparent lattice strain and the apparent crystalline particle size changed discontinuously near 12.5 and 45 hours.

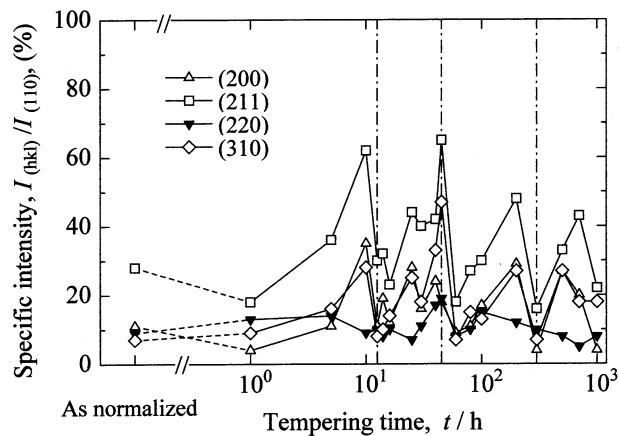


Fig. 3—Specific diffraction intensity as a function of tempering time at 750 °C.

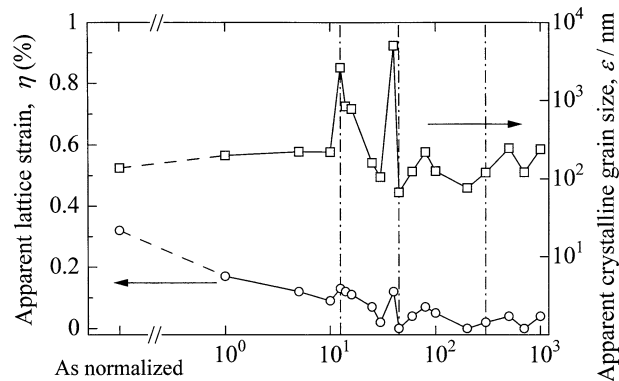


Fig. 4—Apparent lattice strain and apparent crystalline grain size as a function of tempering time at 750 °C.

## B. Precipitation Phenomena

### 1. XRD analyses of the extracted residue

Figure 5 shows the XRD analysis of for the extracted residue from the NBN2 tempered at 750 °C for 100 hours. As shown in the figure, the precipitation of not only MX but also hexagonal Cr<sub>2</sub>N was confirmed. The diffraction angles for the MX peaks were near the peak angles of the cubic CrN or VN. The diffraction angles for the cubic NbN were 1 to 3 deg smaller than the observed peaks of the MX. All the MX peaks appeared broadened, although the (111) and (200) peaks of MX overlapped with the peaks of the Cr<sub>2</sub>N. Detailed discussion is given in Section III-B-4-a. Peaks from other phases, *e.g.*, the tetragonal Z phase,<sup>[27]</sup> were not detected, except for the peaks for the NaCl, which was used as a reference material.

### 2. ICP-AES analysis of the extracted residue

The amount of the extracted residue and the Cr, V, and Nb contents in the residue are shown as a function of tempering time at 750 °C, in Figure 6. As shown in the figure, the amount of the extracted residue and Cr content seemed to reach an equilibrium value, *i.e.*, a value for 1000 hours, by tempering for only 1 hour at 750 °C, but the amounts of V and Nb gradually increased and the precipitation appeared incomplete, even after tempering for 1000 hours. Moreover, the following characteristics were found from Figure 6: (1) the crest and trough were found in the amount of the precipitate and Cr and Nb content curves at the times of the occurrence of the discontinuous changes in hardness at 750 °C, as shown in Figure 2; and (2) the total amount of the extracted residue and Cr content increased markedly at 100 hours of tempering, although the corresponding hardness change was not found in Figure 2.

The decreases observed in the total amount of the residue and Cr content near 12.5 and 45 hours clearly indicated that chromium, which was a major constituent

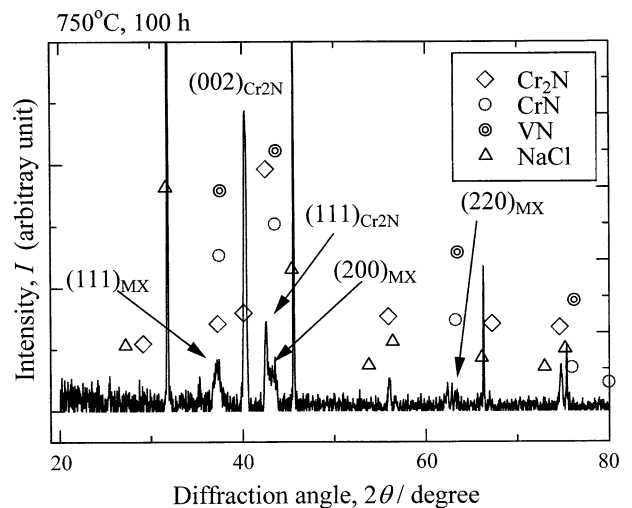


Fig. 5—XRD intensity of extracted residue of tempered NBN2 at 750 °C for 100 h. NaCl powder was used as reference material.

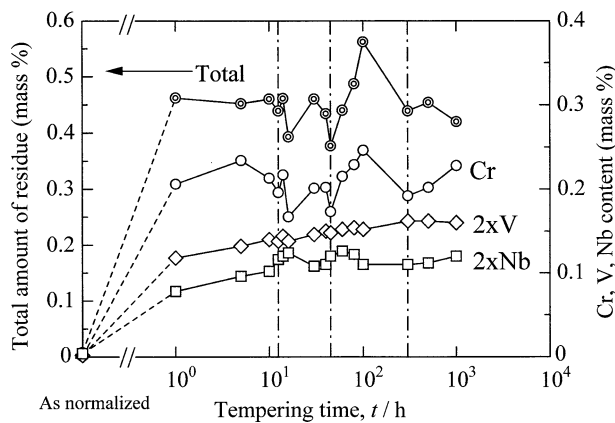


Fig. 6—Results of ICP-AES analysis of extracted residue as a function of tempering time at 750 °C.

metallic element, dissolved temporarily, followed by reprecipitation. On the contrary, two small peaks observed in the Nb content curve obviously indicated that the amount of the MX, and not the  $\text{Cr}_2\text{N}$ , increased intermittently, followed by dissolution at these times, because Thermo-Calc (TC, Thermo-Calc Software, Stockholm, Sweden)<sup>[22]</sup> showed that the  $\text{Cr}_2\text{N}$  could dissolve only a very small amount of the Nb.

Similar results, as shown in Figure 6, had been confirmed in the previous tests. It was surprising that the total amount of the extracted residue or Cr content in the residue varied largely and repeatedly. The reasons were as follows: we had known that the V and Ta content in the residue of martensitic steels, which precipitated VN and TaC, respectively, varied within a short interval near the time of the occurrence of the discontinuous change in hardness during tempering, although we did not take notice of the changes in the amount of the extracted residue and Cr content, because the changes were not very remarkable.<sup>[16,17]</sup> Therefore, in the next step, the changes in the amount of the extracted residue were examined precisely, using an experimental steel that precipitated only  $\text{M}_{23}\text{C}_6$  during tempering; we found that the amount of the extracted residue that was formed in the early stages of tempering decreased at two different times.<sup>[26]</sup> Therefore, the results shown in Figure 6 were the final results in an experiment program that included systematic observations on other properties using NBN2 with the same heat histories. The times of the occurrence of the discontinuous changes in the chemical composition of the residues varied subtly, depending on the heat history, but we had confirmed that the discontinuous changes in the total amount of the residue, Cr, and Nb content curves occurred more than two times within 100 hours' tempering. The detectable limit of the ICP-AES analysis was 0.01 pct; the relative error of the total amount of residue, Cr, V, and Nb content was roughly  $\pm 0.5$ , 2, 5, and 10 pct, respectively. The range of each relative error corresponded to roughly one or two times the size of each symbol. Therefore, the crest and trough measured by ICP-AES shown in Figure 6 were thought to be reliable.

### 3. Transmission electron microscopy observation

Figure 7 shows transmission electron microscopy (TEM) micrographs of the extracted replicas of NBN2 tempered at 750 °C for 100 hours. Two kinds of precipitates, large and small ones, were observed. These results agreed with the results of the XRD analysis shown in Figure 5. The  $\text{Cr}_2\text{N}$  was large; the average particle size was 411 nm, ranging from 190 to 793 nm, with an average aspect ratio of about 1.7. On the other hand, the MX was very fine; the average particle size was 60 nm, ranging from 22 to 166 nm, with an average aspect ratio of about 1.5. These precipitates formed a line, in many cases, which indicated that these compounds precipitated on grain, packet, block, lath, and subgrain boundaries. Analyses by TEM-EDS were also completed for some particles and notations of X, M, Nb, and Cr (in the figure, denoted  $\text{Cr}_2\text{N}$ , (Cr,V,Nb)N, Nb-rich MX, and Cr-rich MX, respectively). In many cases, the contrast of each MX particle was uniform and a complex compound of MX, the so-called V wing,<sup>[28]</sup> was not observed in this steel. Figure 8 shows the chemical composition of the metallic elements of the extracted particles for NBN2 tempered at 750 °C for 100 hours, in order of their Cr content. In summarizing the EDS data, particles with an Si, Al, or Mn content larger than 2 at. pct were omitted, because the

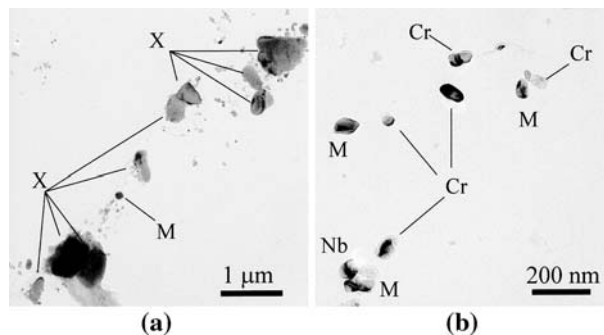


Fig. 7—TEM micrographs of an extracted replica for NBN2 tempered at 750 °C for 100 h: (a) large particles of  $\text{Cr}_2\text{N}$  and (b) fine particles of MX. Notations of X, M, Nb, and Cr denote  $\text{Cr}_2\text{N}$ , (Cr,V,Nb)N, Nb-rich MX, and Cr-rich MX, respectively.

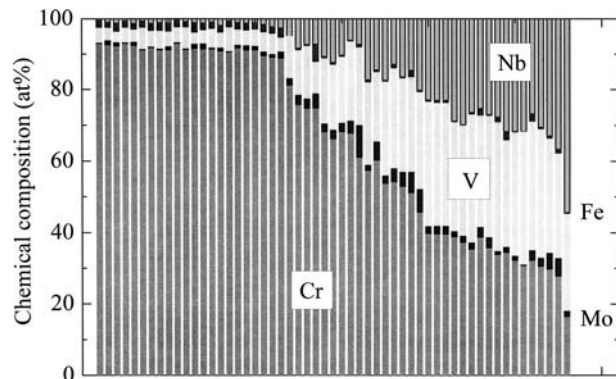


Fig. 8—Results of TEM-EDS analyses of extracted particles on replica for NBN2 tempered at 750 °C for 100 h.

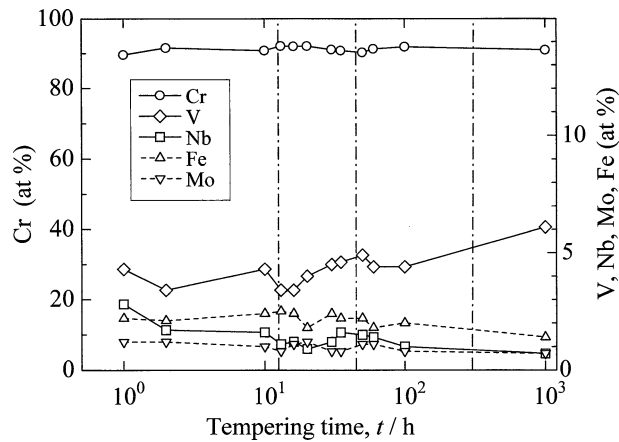


Fig. 9—Tempering time dependence of Cr, V, Nb, Fe, and Mo contents in extracted  $\text{Cr}_2\text{N}$  particles using TEM-EDS.

assessment of their chemical composition might be interfered with by neighboring nonmetallic inclusions or they might have precipitated on nonmetallic inclusions; in the latter case, the particle size might be incorrect. When the particle size was very fine or the particles coagulated with each other, measurement was not done. The major constituent metallic elements of the particles were Cr, V, and Nb, with a small amount of Fe and Mo. We can see two kinds of phase in Figure 8. The chemical composition of the very high Cr phase (left side) had a roughly constant composition. On the other hand, the chemical composition of the other particles varied continuously in a wide range. The former and the latter corresponded to the  $\text{Cr}_2\text{N}$  and the MX, respectively. According to the TC,<sup>[22]</sup> the  $\text{Cr}_2\text{N}$  could dissolve a small amount of Fe and Mo, but the MX could hardly dissolve Fe or Mo. However, Figure 8 shows that the MX dissolved an average of about 3 pct of the Mo. Similar levels of Mo and Fe were detected in the MX in the normalized state, in which only MX can precipitate; therefore, the detected Mo and Fe in the MX shown in Figure 8 should be inherent and the values are thought to be reliable.

Figure 9 shows the chemical composition of the extracted  $\text{Cr}_2\text{N}$  particles, determined using TEM-EDS as a function of tempering time at 750 °C. The chromium content was very high and was roughly constant at 91 pct throughout the tempering duration. The vanadium content of the  $\text{Cr}_2\text{N}$  increased; the Nb, Fe, and Mo content, however, decreased, in general, with the increasing tempering time. It was also found that the Cr content slightly increased, whereas the V and Nb content decreased when the tempering time was 12.5 hours, *i.e.*, at the time of the occurrence of the discontinuous hardness change. On the contrary, the Cr content slightly decreased, and the V and Nb content increased, when the tempering time was 45 hours.

The average Cr, V, and Nb content in the MX particles is summarized in Figure 10 as a function of tempering time at 750 °C. The Mo and Fe contents were omitted for simplicity. The Cr content decreased, and the V and Nb content increased, in general, with the increasing tempering time at 750 °C. The Cr content and

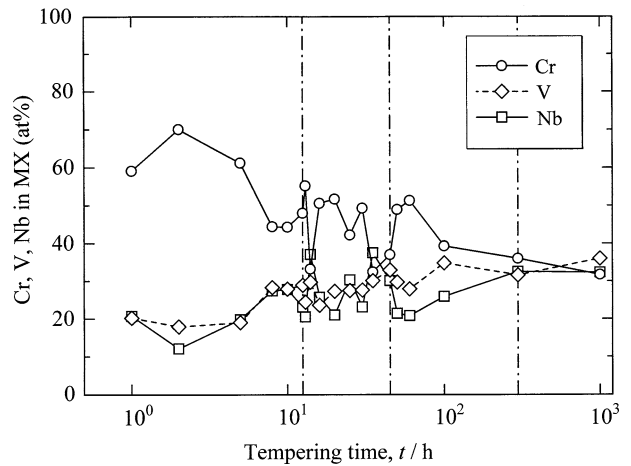


Fig. 10—Tempering time dependence of Cr, V, and Nb contents of the extracted MX particles using TEM-EDS.

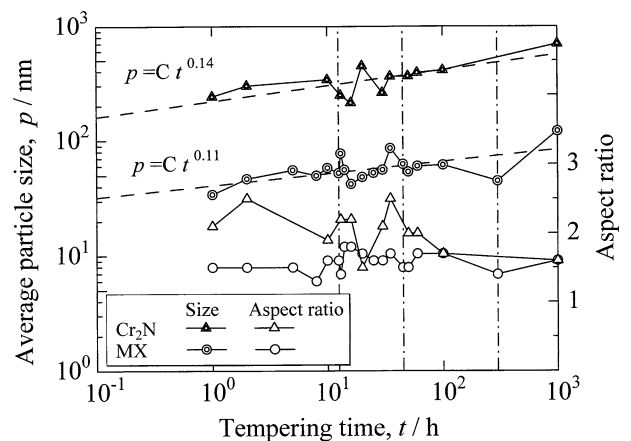


Fig. 11—Tempering time dependence of particle size and aspect ratio of  $\text{Cr}_2\text{N}$  and MX, using TEM-EDS.

the Nb content discontinuously changed several times and were compensative with each other, although the changes in the V content were moderate. When a discontinuous hardness change was observed at 12.5 hours, the Cr content of the MX decreased suddenly, followed by a rapid increase, while the Nb content showed a peak at that time. On the contrary, for the second hardness change, *i.e.*, at 45 hours, the Cr content increased and the Nb content decreased.

The particle size and aspect ratio on the extracted replica were also measured, in addition to the TEM-EDS data; the averaged values for the observed particles (particles with an Al, Si, and Mn content lower than 2 pct) are plotted in Figure 11. The particle size of the  $\text{Cr}_2\text{N}$  and MX gradually increased with the increasing tempering time at 750 °C; the aspect ratio of the  $\text{Cr}_2\text{N}$  decreased with the increasing tempering time, and the aspect ratio of the MX remained roughly constant, in general, throughout the tempering duration. The average time exponent of the particle size for the  $\text{Cr}_2\text{N}$  was 0.14; this value was slightly larger than that for the MX, *i.e.*, 0.11.

#### 4. XRD observation

a. *Precipitation behavior of MX.* As shown in Figure 10, the chemical composition of the MX particles varied with the tempering time at 750 °C and, as shown in Figure 5, the (220) diffraction peak of MX was broadened as compared with the Cr<sub>2</sub>N peaks; thus, this peak was considered to be a complex peak composed of several subpeaks. Although the intensity of the (111) and (200) peaks of the MX were rather strong, they overlapped with the diffraction peaks of the Cr<sub>2</sub>N. Therefore, the profile of the (220) peak of the MX was investigated in detail; the results are shown in Figure 12. The diffraction angle was corrected using NaCl powder and the strongest peak was normalized to a similar height. At the early stages of tempering, a peak was observed at only about 63.2 deg. A subpeak was confirmed at about 62.2 deg after tempering for 16 hours, the high-angle peak began to diminish, and, finally, only the low-angle peak was observed. The peak profile for 45 hours' tempering was complex, as compared with the other peak profiles; a similar result was confirmed by retesting, but the reason for this was not clear.

The observed peak was resolved into three subpeaks by the following method. Figure 13 shows an example

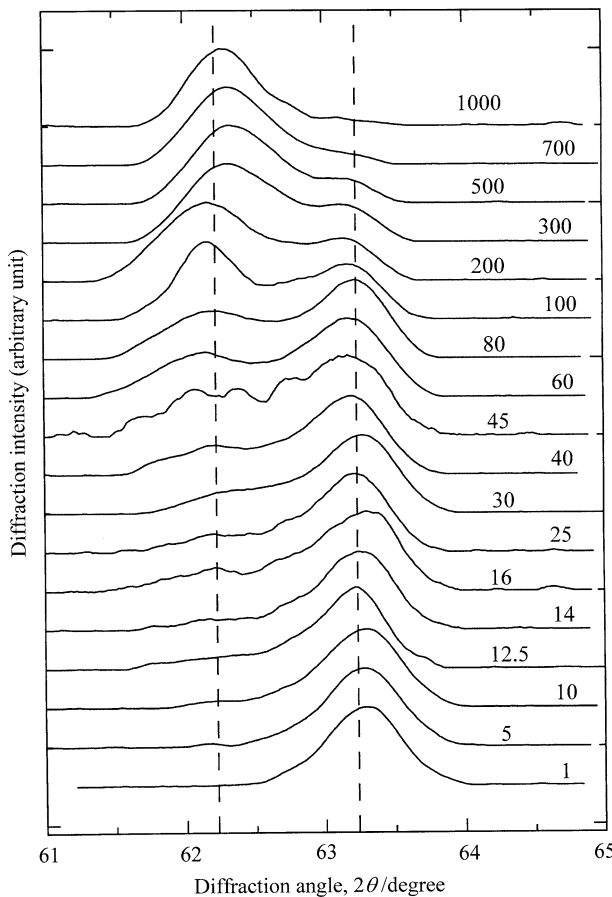


Fig. 12—Diffraction intensity of MX (220) peak as a function of tempering time at 750 °C. Tempering time is shown next to each peak in hours.

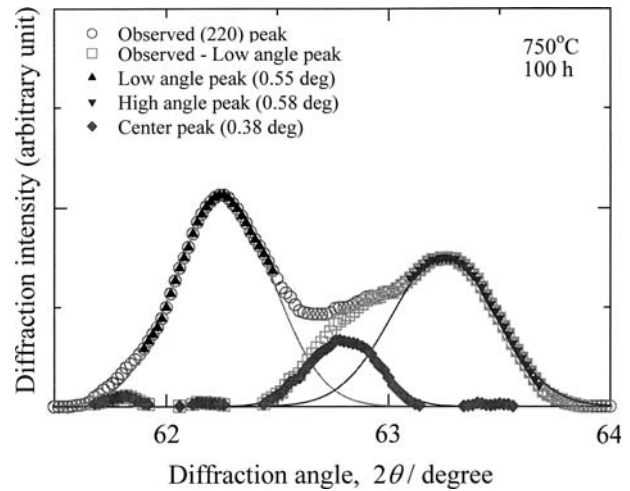


Fig. 13—Illustration of resolution of MX (220) peak of specimen tempered at 750 °C for 100 h. Numbers in parentheses denote calculated integral breadth in degrees ( $b$  in Eq. [2]).

of a specimen tempered at 750 °C for 100 hours. First, data for a major peak, *i.e.*, a low-angle peak, in this case, were selected in a way similar to that shown in the figure. It is well known that the summit portion of an XRD peak can be well fitted by a normal distribution curve. Therefore, the selected data were fitted by the following equation:

$$y = a \exp \left\{ -\pi \left( \frac{x - c}{b} \right)^2 \right\} \quad [2]$$

where  $y$  and  $x$  are the diffraction intensity (arbitrary unit) and diffraction angle (degree), and  $a$ ,  $b$  and  $c$  are the peak height (arbitrary unit), integral breadth (degree), and peak diffraction angle (degree), respectively. Next, the calculated intensity for the low-angle peak was subtracted from the observed data and the subtracted intensity data were plotted. Then, data for a high-angle peak were newly selected from the replotted data; the newly selected data were fitted by a normal distribution curve again. Finally, by subtracting the calculated intensities for the low- and high-angle peaks from the observed data, we found the residual peak at a middle angle of the two subpeaks, as shown in Figure 13. The observed peak profile for the (220) peak of the MX shown in Figure 12 could be explained by the presence of three subpeaks, which were caused by the high-, low-, and middle-angle MX particles.

The relative intensity,  $I_H/I_O$ ,  $I_L/I_O$ , and  $I_M/I_O$ , is plotted in Figure 14(a). The subscripts O, H, L, and M denote the observed, high-, low-, and middle-angle subpeak, respectively. The integrated intensity  $I_O$  is the observed integrated intensity, and the  $I_H$ ,  $I_M$ , and  $I_L$  are given by the product of the peak height and the corrected integral breadth, using standard Si powder, because the integral of Eq. [2] from  $-\infty$  to  $+\infty$  is  $a \times b$ . It was confirmed from Figure 14 that the relative intensity of the high-angle peak decreased, in general, after 10 hours' tempering at 750 °C; the intensity of the low-angle peak increased, instead; and the intensity of

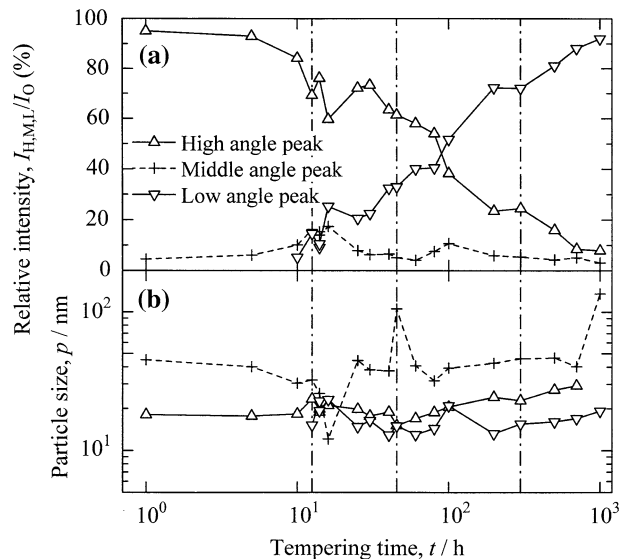


Fig. 14—Relative intensity of the resolved peaks, *i.e.*, high-angle, low-angle, and center peaks for MX (220) peak, as a function of tempering time at 750 °C. The particle size calculated from integral breadth for each resolved peak is plotted in the bottom figure.

the middle-angle peak stayed at rather low levels, although the discontinuous changes were seen after near 20 hours' tempering.

When a crystalline particle is cubic and the size is uniform, the particle size can be estimated from the integral breadth, using the Scherrer's relation.<sup>[24]</sup> Although the MX particles precipitated in this alloy were not cubic and their size was not uniform, as shown in Figure 7, in this study, the average size of the MX was estimated using the Scherrer's relation; furthermore, for the sake of simplicity, the particle size of the MX was assumed to be equal to the crystalline particle size. The calculated particle sizes from each peak are plotted in Figure 14(b). The particle size for the high-angle MX gradually increased, ranging from 20 to 30 nm; the particle size for the low-angle MX was rather small, about 20 nm. On the other hand, the middle-angle MX was rather large, about 50 nm. The size of the middle-angle MX changed discontinuously at tempering times of 20 and 45 hours, as shown in the figure.

The same assumptions were made for an 8 pct Cr-2 pct WTa steel; a fair correspondence between the particle size of both the  $M_{23}C_6$  and TaC particles observed by TEM and measured by XRD was confirmed.<sup>[17]</sup> However, in the case of this steel, NBN2, the correlation between the particle size of the MX measured by TEM (Figure 11) and XRD (Figure 14) was not very good. The particle size of the MX at 1000 hours as measured by TEM was about 100 nm, but the particle size for the major subpeak, *i.e.*, the low-angle MX, was about 20 nm. This discrepancy will be discussed in Section IV-A-5.

The interplaner distance of the high-angle MX can be calculated from the diffraction angles shown in Figure 12. The average was 0.1470 nm, after correction by NaCl powder. This value was close to the interplaner distance of the (220) plane of cubic CrN (0.14665 nm,

powder diffraction file (pdf) card no. 01-077-0047), rather than those of the other MX nitrides. The interplaner distance of the low-angle MX averaged 0.1491 nm, after correction by NaCl powder, and was larger than that of the high-angle MX, *i.e.*, CrN. The interplaner distance of the low- and high-angle MX changed subtly around each average interplaner distance with increases in tempering time. As shown in Figure 10, the V content and the Nb content in the MX increased with the increase in tempering time, but there was no reliable pdf card directly corresponding to these chemical compositional changes. It may be noted that the pdf card nos. 03-065-5011, 03-065-0436, 01-074-1218, 01-071-0162, 01-077-0047, 00-035-0768, 03-065-7236, 03-065-5288, 03-065-4307, 01-089-7381, 01-089-5265, 01-078-1315, 01-073-2038, 01-073-0528, 01-077-0048, and 01-089-5136 show the following relation:

$$d_{\text{NbN}}(0.15543) > d_{(\text{Nb,V})\text{N}}(0.15118) > d_{\text{CrN}}(0.14665) > d_{(\text{Cr,V})\text{N}}(0.14634) > d_{\text{VN}}(0.14615) \quad [3]$$

where  $d_{\text{NbN}}(0.15543)$  denotes the (220) interplaner distance of the NbN (nm), *etc.* This relation directly indicates that Nb increases the lattice constant of CrN, whereas V decreases it slightly. The expansion and contraction of the MX lattice will depend on the content of Nb and V. Since the (220) peak angle shown in Figure 12 shifted to a lower value with an increase in tempering time, it can be implied that this shift may be caused by an increase in the Nb content of the MX and not by the V content.

*b. Precipitation behavior of  $\text{Cr}_2\text{N}$ .* The diffraction intensity of a  $\text{Cr}_2\text{N}$  (002) peak can be also fitted by Eq. [2]. However, a peak profile spread into a low-angle side in the later stage of tempering, and the fitness became poor. Therefore, a diffraction peak was resolved into two subpeaks, as in the case of the MX (Figure 13). An example is shown in Figure 15. In the case of the  $\text{Cr}_2\text{N}$ , the difference of the resolved peak angles is 0.1 to 0.2 deg at the most, in contrast to the case of the MX. Therefore, the high-angle data, which corresponded to a peak observed at the early stages of tempering, were first selected by trial and error. These data were fitted by a normal distribution curve. Then, the residue, *i.e.*, the observed intensity minus the calculated intensity, was fitted again, and a low-angle peak was obtained. The calculated material constants  $a$ ,  $b$ , and  $c$ , obtained using Eq. [2] for each peak, were converted to the relative intensity, particle size, and interplaner distance, respectively. Both interplaner distances,  $d_{002}$ , for a major high-angle  $\text{Cr}_2\text{N}$  peak and a minor low-angle peak are shown in Figure 16(a). The interplaner distance of the high-angle (002) peak of the  $\text{Cr}_2\text{N}$ , observed by tempering at 750 °C for 1 hour, was 0.22366 nm; this value was close to the value of the  $\text{Cr}_2\text{N}$  of 0.22419 nm (pdf card no. 00-035-0803) rather than of 0.22145 nm (pdf card no. 01-079-2159). The value of  $d_{002}$  for the high-angle  $\text{Cr}_2\text{N}$  increased with an increase in the tempering time, and reached 0.22430 nm when the tempering time was 1000 hours. Although this value was still close to the  $d_{002}$  of the former standard  $\text{Cr}_2\text{N}$ , *i.e.*, 0.22419 nm, the



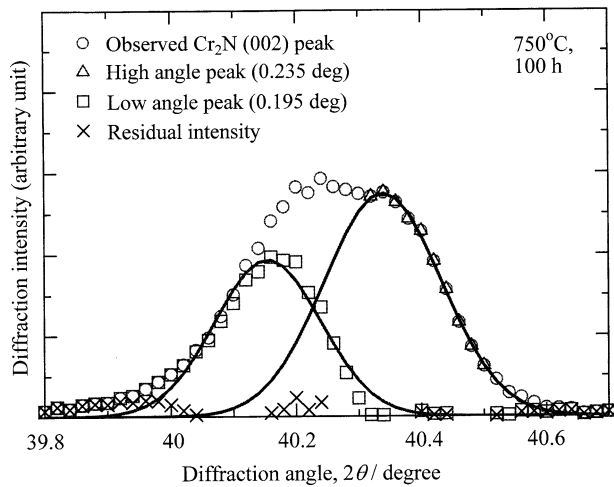


Fig. 15—Illustration of resolution of  $\text{Cr}_2\text{N}$  (002) peak of specimen tempered at 750 °C for 100 h. Numbers in parentheses denote calculated integral breadth in degrees.

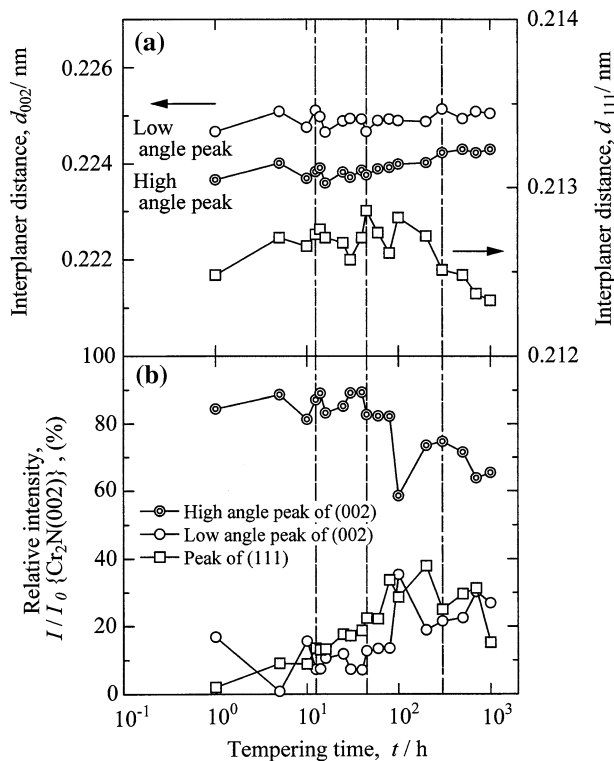


Fig. 16—Analysis results for (002) and (111) peaks of  $\text{Cr}_2\text{N}$  as a function of tempering time at 750 °C. Interplanar distance for  $d_{200}$  and  $d_{111}$  is plotted in upper figure; relative intensity is plotted in lower figure.

observed increase in  $d_{002}$  was thought to be significant. This increase in  $d_{002}$  should be correlated with the increase in the V content or the decrease in the Nb content, as shown in Figure 9. Unfortunately, the microalloying effect of V and Nb on the hcp lattice parameter of the  $\text{Cr}_2\text{N}$  was not available in the pdf card system. However, pdf card nos. 01-079-2159, 00-035-0803, 00-033-1439, 00-040-1274, 01-075-0952, 01-075-1616, and 01-089-5129 show the following relation:

$$d_{\text{Nb}_2\text{N}}(0.24800) > d_{\text{V}_2\text{N}}(0.22840) > d_{\text{Cr}_2\text{N}}(0.22282) \quad [4]$$

where  $d_{\text{Nb}_2\text{N}}(0.2480)$  denotes the interplaner distance of the (002) plane of the  $\text{Nb}_2\text{N}$  (nm), etc. This relation, combined with Vegard's law, led to the conclusion that the observed increase in the V content and the decrease in the Nb content in the  $\text{Cr}_2\text{N}$  could explain the expansion of the (002) interplaner distance of the observed  $\text{Cr}_2\text{N}$  compound, if the expansion due to the increase in the V content were much larger than the shrinkage due to the decrease in the Nb content. However, this was not the case, as is shown in Figure 9. Therefore, the reason for the increase in the interplaner distance of the high-angle  $\text{Cr}_2\text{N}$  was unclear.

The relative intensity,  $I/I_0\{\text{Cr}_2\text{N}(002)\}$ , where  $I$  denotes the integrated intensity of a low- or high-angle  $\text{Cr}_2\text{N}$  peak and  $I_0\{\text{Cr}_2\text{N}(002)\}$  means the observed entire integrated intensity for a  $\text{Cr}_2\text{N}$  (002) peak is shown in Figure 16(b). The relative intensity of the high-angle peak decreased gradually with the advance of the tempering; on the other hand, the relative intensity of the low-angle peak increased.

In Figure 16, the interplaner distance and relative intensity of the  $\text{Cr}_2\text{N}$  (111) peak are also plotted. These values were calculated by applying Eq. [2] only to the summit portion of the  $\text{Cr}_2\text{N}$  (111) peak, because the  $\text{Cr}_2\text{N}$  (111) peak overlapped with the MX (200) peak (Figure 5). The value of  $d_{111}$  of the  $\text{Cr}_2\text{N}$  increased up to about 100 hours and then decreased. The changes in the interplaner distance of the  $\text{Cr}_2\text{N}$  (002) and (111) peaks implied that the  $c/a$  of the hcp lattice changed during tempering. The hcp lattice expanded three dimensionally until 100 hours' tempering at 750 °C and then the  $c/a$  ratio increased at the later stages of tempering.

## IV. DISCUSSION

### A. Growth Kinetics of Precipitates

#### 1. Remeasurement of particle size by TEM

In order to estimate the long-term creep strength of high-strength, nitrogen-bearing steels, it is important to evaluate the growth kinetics of MX and  $\text{Cr}_2\text{N}$ . The particle sizes measured by TEM and XRD are shown in Figures 11 and 14, but the two sets of data did not agree with each other. One reason for this was that the XRD measurement was based on many assumptions. On the other hand, in the TEM observation, the results of which are shown in Figure 11, the EDS analysis took priority, and the size of all particles was not measured. The particle sizes shown in Figure 11 were measured only for the particles that were judged to be  $\text{Cr}_2\text{N}$  or MX by TEM-EDS. Small particles and particles that were affected by nonmetallic inclusions were excluded. Therefore, the particle size shown in Figure 11 might be biased toward larger sizes; also, the total number of particles measured was not very large. Therefore, the size measurement was conducted again for all particles, indiscriminately, on recorded images, until the total number of particles was one order of magnitude larger than that of Figures 8 through 10, although EDS

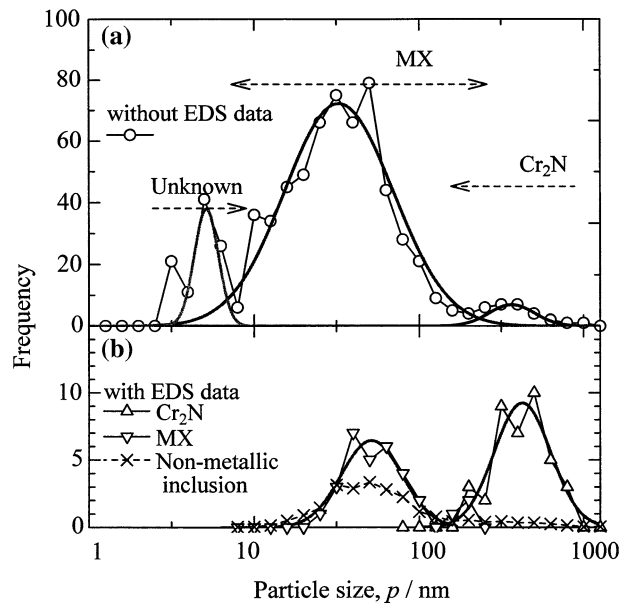


Fig. 17—Histogram of particles precipitated on replicas in specimen tempered at 750 °C for 100 h: (a) upper figure shows histogram for all data measured on replicas and (b) lower figure shows histograms for Cr<sub>2</sub>N, MX particles and nonmetallic inclusions distinguished by TEM-EDS analysis.

measurements were not done. Figure 17(a) shows a size histogram for the remeasured particles tempered at 750 °C for 100 hours. Particle-size histograms with EDS data are shown in Figure 17(b); both histograms, for the Cr<sub>2</sub>N and the MX, followed an approximately lognormal distribution curve. In Figure 17(b), the frequency distribution for nonmetallic inclusions, the definition of which was a particle that had more than 2 at. pct of Al, Si, or Mn, is also shown. The frequency of inclusions, especially with larger sizes, was limited and was scattered. Therefore, the average frequency, *i.e.*, the total number of all nonmetallic inclusions measured in this study divided by the number of measurements, was plotted by cross marks in Figure 17(b).

A histogram for the remeasured particles shown in Figure 17(a) followed an approximately lognormal distribution curve of a trimodal type. Referring to the data developed from EDS analysis, it could be concluded that the right and center peaks correspond to the Cr<sub>2</sub>N and the MX, respectively. In addition to these peaks, we could see a peak with a very fine particle size, below 10 nm, but we could not identify the compound. The histogram of the remeasured particle size included nonmetallic inclusions. However, as shown in Figure 17(b), the peak sizes for the MX and the nonmetallic inclusions were similar to each other. Therefore, we determined that the average particle size of a specimen tempered for 100 hours at 750 °C for the Cr<sub>2</sub>N and the MX was 289 and 28 nm, respectively, by applying lognormal distribution curves to the right and center peaks. These sizes were smaller than the sizes measured by including only particles assessed using EDS analysis, at 368 and 46 nm, for the Cr<sub>2</sub>N and the MX, respectively.

## 2. Comparison of particle size measured by TEM and XRD

The remeasured particle sizes of the Cr<sub>2</sub>N and the MX (Figure 17) are plotted as a function of tempering time in Figure 18. In the figure, the particle sizes of the high-angle and low-angle MX peaks measured by XRD were also replotted from Figure 14; in addition, the particle sizes of the Cr<sub>2</sub>N calculated from the integral breadth of the major high-angle (002) peak and the (111) peak were plotted. Since the (111) peak of the Cr<sub>2</sub>N overlapped with the MX (200) peak, the summit of the (111) peak was separated from the observed combined peak; then, it was fitted by a bimodal lognormal distribution curve and, finally, the calculated integral breadth for the high-angle subpeak of the Cr<sub>2</sub>N (111) peak, which was resolved using a method similar to that used for the (002) plane shown in Figure 15, was converted to the particle size. It was found from the figure that the particle size of the Cr<sub>2</sub>N measured from a major (002) peak or a (111) peak was comparable to that by measured by TEM at short and long tempering times and was about 1/4 of the TEM data in between, which depended on the tempering time and diffraction peak used.

It was also found that, although the particle size of the MX calculated from the high-angle (220) peak agreed with the TEM data until 25 hours, the XRD size data were about 2/3 of the TEM size data when the tempering time was longer than 45 hours; it was also found that the particle size measured from the low-angle (220) peak, which was formed in the later stages of tempering, was about 1/3 of the TEM size data.

## 3. Determination of the amounts of Cr<sub>2</sub>N and MX and the Composition of MX

The number of precipitates in the high-Cr martensitic steels, which precipitated only carbides, *i.e.*, M<sub>23</sub>C<sub>6</sub> and

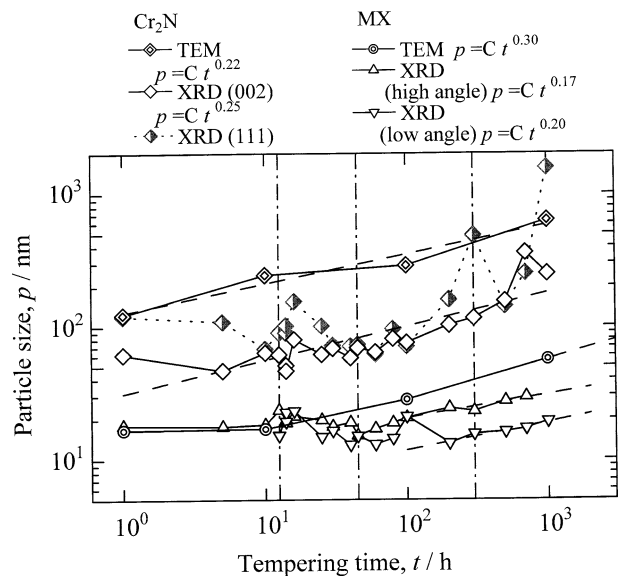


Fig. 18—Particle size of Cr<sub>2</sub>N and MX measured by TEM and XRD as a function of tempering time at 750 °C.

MX carbide, could be estimated from the mass content data of the Cr, V, and Nb in the residue, because the  $M_{23}C_6$  hardly dissolved the V and Nb, and the MX carbide hardly dissolved the Cr. On the contrary, in the case of the N-bearing steel, since the MX nitride dissolved a considerable amount of the Cr, in order to determine the amount of each compound, the target compounds should be collected separately for the XRD measurements. However, a technique such as selective electrolyzing does not exist, and so the estimation for the amount of precipitates was done as follows.

The chemical composition of the extracted residue measured by ICP-AES (Figure 6) was converted to the chemical composition of the MX. This assumes, first, that the major constituent elements of MX were Cr, Nb, V, and N and that the  $Cr_2N$  contained only Cr and N; second, that the total amount of the N was in the  $Cr_2N$  or the MX; and, finally, that both the  $Cr_2N$  and the MX were stoichiometric compounds. The amount of  $Cr_2N$  and MX estimated from the calculation described here could also be estimated from the observed total amount of the extracted residue. The observed compounds, MX and  $Cr_2N$ , contained small percentages of Fe and Mo, but the amount of these elements in the residues was not measured. Therefore, in order to solve the uncertainty that might arise from the unmeasured elements and nonmetallic inclusions, the adjustable parameter,  $\alpha$ , was introduced. When  $\alpha = 1.08$ , the mass of the observed extracted residue was equal to  $\alpha$  times the summation of the calculated mass of the  $Cr_2N$  and the MX and the amount of the observed residue in the normalized state. The amount of the observed residue in the normalized state corresponded to the volume of the nonmetallic inclusions (0.008 wt pct). This result,  $\alpha = 1.08$ , meant that 8 pct of the extracted residue contained minor constituent elements in total (Fe, Mo, Si, Al, Mn, etc.), which might be an acceptable assumption, referring to Figures 8 and 9. The calculated results are shown in Figure 19. These results showed, first, that the major precipitate was MX nitride; its amount was about 0.3 pct and it decreased slightly, accompanied by crest and trough, with the increase in tempering time. Second,

the calculated results of the major constituent elements, Cr, V, and Nb, were similar to the EDS results shown in Figure 10, but the values of the Nb content in the MX were about half of the values measured by TEM-EDS. The difference in the Nb content might be caused by analytical error; the value of the EDS might be responsible for the difference, because the compound contained a small amount of Mo and the wavelengths of Mo and Nb were very close to each other. Although the unknown elements of the 8 pct were not analyzed precisely ( $\alpha = 1.08$ ) and about 5 pct of the V in the  $Cr_2N$  (per the EDS data) was ignored in the estimated results shown in Figure 19, the analytical errors in the estimation were considered to be comparable to those of ICP-AES, as described in a Section III-B-2. Therefore, the amount of  $Cr_2N$  and MX and the chemical compositions of the MX calculated from the ICP-AES data (Figure 19), rather than those calculated by TEM-EDS, were thought to be of significance for further discussion.

#### 4. Particle size of $Cr_2N$

In regard to the growth of the  $Cr_2N$ , the particle size measured by TEM was rather larger than that measured by XRD (Figure 18). Though the TEM data obtained by direct measurement were valid, there was a problem: the very fine particles were easily covered by or would attach to larger particles. On the other hand, in the case of XRD, although the data were valid, there was a problem in simply applying the Scherrer's relation, because the calculated size was an average value of more than  $10^{10}$  particles of varying sizes. As shown in Figure 5, the peak height of a basal plane of  $Cr_2N$  in the extracted residue using an aspirator was extremely high, as compared to that of the (111) peak, which should be the highest peak of randomly oriented powder, as shown in the pdf cards. In order to confirm the orientation of the  $Cr_2N$  in the residue, another extracted residue of the sample shown in Figure 5 was obtained by the following method. The electrolyzed solution of the NBN2 tempered at 750 °C for 100 hours was left in a beaker for a while, and then the top clean layer in the beaker was replaced by fresh alcohol. After repeating this process and drying the solution, we finally obtained a deposit in the bottom of the beaker. The deposit was examined using XRD. We confirmed that the measured intensities of the  $Cr_2N$  in the residue were proportional to those of the pdf cards. This implied that the extracted  $Cr_2N$  powder on a filter using an aspirator was like a plate lying on the filter the surface of which was parallel to a basal plane, although direct observations of the filters by TEM or SEM were not done. If this speculation were true, the particle size of the  $Cr_2N$  measured from the (002) peak, *i.e.*, the thickness of the particles perpendicular to the (002) plane, seemed to be small, as compared to the average size. On the other hand, the accuracy of the particle size measured from the (111) peak was not very high, because the MX (200) peak interfered with the (111) peak of the  $Cr_2N$ . However, at either the early or the later stages of tempering, the peak profile of the MX was simple (Figure 12) and could be easily resolved to a complex

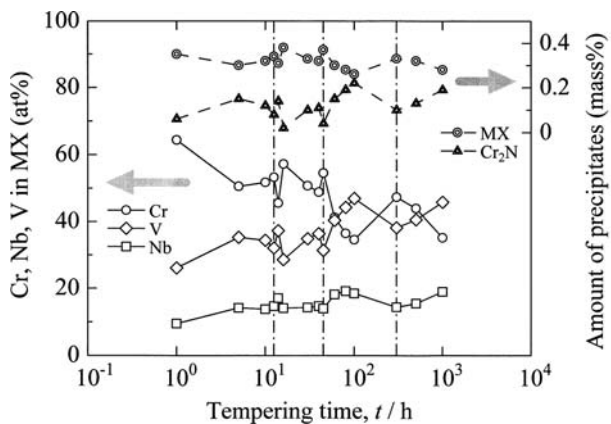


Fig. 19—Cr, Nb, and V content in MX and amount of precipitates as a function of tempering time at 750 °C calculated from ICP-AES data.

triplet diffraction peak; therefore, in these cases, the observed values were rather reliable, as compared to the middle stage of tempering. If the extracted  $\text{Cr}_2\text{N}$  particles were platelike, the TEM image shown in Figure 7(a), which was used to measure the particle size, suggested that the observed particle size measured by TEM was apparently larger than the real average values. In the case of  $\text{M}_{23}\text{C}_6$ , previous work<sup>[17]</sup> showed us that the particle sizes measured by TEM and XRD agreed with each other. Therefore, the average particle size of real  $\text{Cr}_2\text{N}$  particles might be between the values estimated using TEM and XRD.

The amount of  $\text{Cr}_2\text{N}$  shown in Figure 19 increased gradually with crest and trough, and did not saturate, even after tempering at 750 °C for 1000 hours. The size of the  $\text{Cr}_2\text{N}$  gradually increased (depending on the measuring method), and the growth curves had crest and trough near 15 hours ((002) and (111) peaks) and 300 hours ((111) peak). The apparent time exponent of the particle size of the  $\text{Cr}_2\text{N}$  was about 0.25.

### 5. Chemical composition and particle size of MX particles

As shown in Figure 18, the particle size of the MX remeasured by TEM increased gradually with an increase in tempering time. These values were just comparable to the XRD data at the early stage of tempering. However, at the later stage of tempering, the particle size measured by TEM was about 3 times larger than the size of the low-angle MX and 1.5 times larger than the high-angle MX. It was reported that, in a similar martensitic steel, in which TaC particles precipitated, the particle size measured by TEM agreed fairly well with the particle size measured by XRD, excluding some larger particles.<sup>[17]</sup> Therefore, in order to explain the difference between the TEM and the XRD data, especially for the MX particles newly formed in the later stage of tempering, additional discussion is necessary.

Figure 20 shows all the individual chemical compositions of the MX with the averaged values of EDS and the calculated values from the ICP-AES data plotted in an Nb-V-Cr ternary diagram. In the figure, the compositions of the  $\text{Cr}_2\text{N}$  and the MX in  $\gamma$  iron are also shown, but the individual data of these compounds were omitted, because these data were located in an extremely narrow range for each. The chemical composition of the MX started from a high-Cr region in the ternary diagram and shifted to a high-V and high-Nb content range, with an increase in tempering time. Individual data were distributed widely around the average position, and the composition did not converge at a certain stoichiometric position, even after tempering at 750 °C for 1000 hours (the cross symbol shown in Figure 20 indicates all individual chemical compositions for 1000 hours).

Suzuki *et al.*<sup>[12]</sup> reported the chemical composition of the fine particles formed in a ruptured specimen of the modified 9Cr steel at 600 °C and 650 °C. They showed that the scattering ranges of the chemical compositions of Nb-rich MX, V-rich MX, and Z phase in an Nb-V-Cr ternary diagram; the compositions of both the V-rich MX and the Z phase were distributed more widely, as

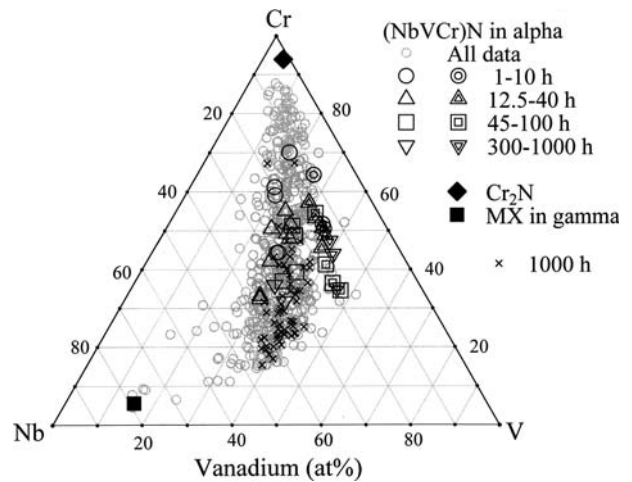


Fig. 20—Distribution of Nb, V, and Cr content of particles precipitated at 750 °C. Small gray circles show composition of all observed data by EDS; cross symbols denote observed data by EDS for 1000 h. Larger open symbols denote average values measured by EDS; larger double symbols denote average values calculated based on ICP-AES data. Solid symbols denote data for average values for  $\text{Cr}_2\text{N}$  and MX in  $\gamma$  iron.

compared to that of Nb-rich MX. The chemical composition of the MX formed in the later stages of tempering in our experiment was near the composition of the Z phase measured at 650 °C by Suzuki *et al.*, but the XRD measurement (Figure 5) clearly showed that the precipitated phase was the cubic MX and not the tetragonal Z phase. Of course, at lower temperatures, the MX phase confirmed in this study might be decomposed into other phases. However, the previous studies and our observations (Figure 20) indicated that MX nitride could dissolve considerable amounts of metallic elements, as compared to MX carbide, and that the miscibility gap between MX nitride and other compounds might not be very distinct, as compared to MX carbide. The accuracy of the chemical composition of the particles extracted on replicas measured by TEM-EDS was not very high, because the measured surface of the particles was not flat and the spectrum was interfered with by neighboring compounds. However, in the case of the MX carbide, scattering in the chemical composition, such as that shown for MX nitride by the cross symbols in Figure 20, was not observed using the same TEM-EDS; the average chemical composition did not change as significantly as shown in Figure 20 with an increase in tempering time.<sup>[15,17]</sup> Therefore, it was thought to be an intrinsic characteristic that MX nitride could dissolve several kinds of metallic elements with different contents at the same time and that the composition of MX might vary with increasing tempering time, balanced with other compounds, *i.e.*,  $\text{Cr}_2\text{N}$ , in this steel.

An MX particle with a specified chemical composition should have a characteristic lattice constant. Therefore, the widely ranging distribution of the chemical composition of the MX in the extracted residue shown in Figure 20 should cause a broadening of the diffraction peak. If this overlapped with the broadening caused by

the decrease in the crystalline particle size, the apparent particle size of the MX should be small. This was one of the possible reasons for the difference in the particle size observed by TEM and XRD. This explanation did not contradict the phase rule and indicated that the precipitation phenomenon did not reach an equilibrium state, even after tempering at 750 °C for 1000 hours. Iseta *et al.*<sup>[29]</sup> studied the precipitation behavior of a high-chromium, nitrogen-bearing martensitic steel using a thin foil and showed that VN particles precipitated in an as-tempered state were platelike. If we assumed that the MX nitride in the present steel, NBN2, was also platelike and that the growth direction was parallel to the plate, since platelike precipitates easily laid down on the extracted replica, the particle size measured by TEM shown in Figure 18 was apparently overestimated; this should be significant when the particle size was large, *i.e.*, in the later stages of tempering. This was the second explanation for the discrepancy between the TEM and XRD observations shown in Figure 18. Finally, the detectable limit measured by XRD might be another reason for the discrepancy; that is, when a diffraction peak was composed of subpeaks, the foot portion of each subpeak interacted with the other portions, and thus, the integral breadth, *i.e.*, the particle size of the MX nitride, would not be measured correctly.

Although the amount of MX slightly decreased with the increase in tempering time, as shown in Figure 19, the MX curve had a similar crest and trough similar to those in Figures 6, 10, and 14. The apparent time exponents of the particle size were 0.3 and 0.2 for TEM and XRD, respectively, when the tempering time was longer than 100 hours. These values were larger than those of MX carbide, *i.e.*, near 0.1.<sup>[12,17]</sup> The high values of the apparent time exponent of the size of the MX nitride observed in this steel agreed with previous work, which showed that the coexisting Cr<sub>2</sub>N in a high-N martensitic steel increased the growth rate of MX.<sup>[15]</sup> However, Sawada *et al.*<sup>[15]</sup> reported that the average size of the MX nitride precipitated in the steel developed by Taneike *et al.*<sup>[13,14]</sup> ruptured at 650 °C and about 10,000 hours was roughly 50 nm. This value was larger than the size of the TaC particles precipitated in a martensitic steel aged at 650 °C for 30,000 hours, which was about 20 to 30 nm.<sup>[30]</sup> In general, the particle size precipitated at the boundaries was larger than that precipitated in a lath martensite or grain. Therefore, these experimental results showed us that MX nitride was easy to precipitate on the lath or subgrain boundaries, but not within the lath martensite or subgrains and, therefore, grew fast, as compared to MX carbide.

## B. Recovery of Microstructure

### 1. Recovery processes

Using the data shown in Figure 2, the apparent activation energy for recovery could be calculated for a state of the same hardness and a state of the occurrence of a discontinuous change in hardness. The apparent activation energy and its 95 pct confidence limits are shown in Figure 21 as a function of the hardness number. First, the hardness data for the same

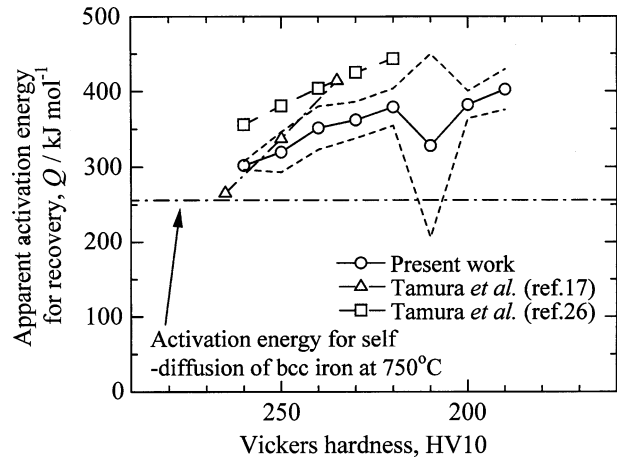


Fig. 21—Apparent activation energy for the recovery of hardness of experimental steel NBN2 and similar martensitic steel, as a function of Vickers hardness; 95 pct confidence limits for NBN2 are given.

temperature shown in Figure 2 were fitted using a smooth curve. The apparent activation energy was calculated for more than three data of tempering time for a given hardness. Extrapolation was not carried out in the calculation. It was found from the figure that the apparent activation energy for the major recovery process, which corresponded to a linearly decreasing part with the logarithm of time in Figure 2, ranged from 302 to 402 kJ/mol and averaged 353 kJ/mol. Since the activation energy for the lattice diffusion of the  $\alpha$  iron was 258 kJ/mol at 700 °C,<sup>[31]</sup> the observed values of the activation energy suggested that the recovery process of martensite was basically controlled by the self-diffusion of the matrix. The apparent activation energies observed for similar steels are also plotted in the figure.<sup>[17,26]</sup> It was found that the apparent activation energy for the recovery of the martensitic steel increased when the hardness decreased, *i.e.*, in the later stages of tempering. Although the detailed mechanism of the complex recovery processes was unclear, the lower values of the activation energy at high hardness might suggest that many dislocations introduced by normalizing assisted the recovery of the martensite through pipe diffusion.

The hardness generally decreased during tempering through a mechanism controlled mainly by self-diffusion; however, as shown in Figure 2, discontinuous hardness changes were observed and the time of the discontinuous point was longer when the tempering temperature was low. This might imply that some thermally activated processes that triggered a discontinuous hardening or softening process were overlapping with the general softening processes. Figure 22 shows the relation between the tempering temperature and the time of the occurrence of the discontinuous changes in hardness. The apparent activation energy for the discontinuous hardness changes was calculated; a value of about 128 kJ/mol (the 95 pct confidence limit ranged from 109 to 146 kJ/mol) was obtained. This was much smaller than the values of the lattice diffusion of the  $\alpha$  iron or of the Cr, Nb, and V diffusion in iron.<sup>[31]</sup> Similar discontinuous hardness changes were also observed in

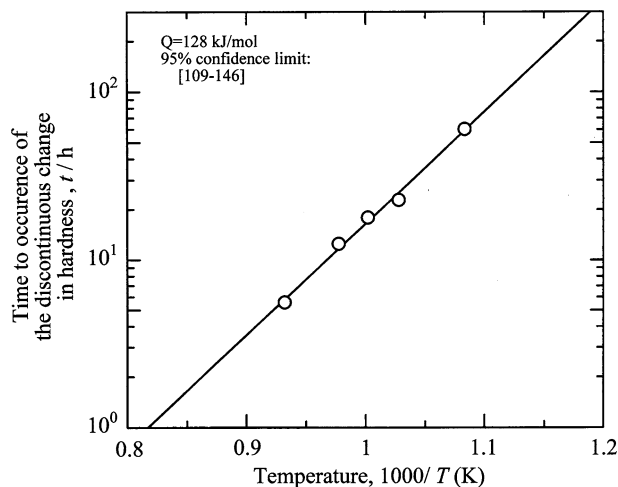


Fig. 22—Relation between tempering temperature and time of occurrence of discontinuous change in hardness (Fig. 2). Apparent activation energy and 95 pct confidence limits are given.

similar martensitic steels; the values of 42 to 152 kJ/mol were reported.<sup>[17,26]</sup> The activation energy for the grain-boundary diffusion of  $\alpha$  iron was about 204 kJ/mol,<sup>[32]</sup> while the activation energy for the diffusion of interstitial nitrogen atoms through the  $\alpha$  iron was 143 to 169 kJ/mol.<sup>[32]</sup> Therefore, these data suggested that a process that caused the discontinuous hardness changes might be related to the diffusion of interstitial atoms.

## 2. Relation between discontinuous reactions and precipitates

Martensitic steel has been thought to soften continuously by processes involving the annihilation of dislocations in lath martensite, the subsequent increase in lath width, and the simultaneously occurring nucleation and growth of subgrains in the middle stages of tempering.<sup>[3]</sup> However, the previous work<sup>[17,26]</sup> on the tempering processes of the similar 9 pct Cr martensitic steels showed that the discontinuous changes in hardness and the preferred orientation measured by XRD occurred consecutively within a short interval. The continuous occurrence of the annihilation of dislocations and the increase in the lath width could not easily explain the discontinuous changes in the preferred orientation. Electron backscattered pattern (EBSP) measurements of the similar 9 pct Cr steel showed that the subgrains began originating at the time of the occurrence of the discontinuous change in hardness or the preferred orientation; the newly formed subgrains seemed to be created independent of the orientation and presence of pre-existent lath martensite.<sup>[26]</sup> In this study, although EBSP or TEM measurements were not done, the discontinuous changes in the preferred orientation by XRD (Figure 3) and the discontinuous hardness changes (Figure 2) were certainly observed at almost the same time. Therefore, the discontinuous changes in hardness could be related to the creation and growth of subgrains during tempering.

The total amount of the extracted residue and hardness changed discontinuously at 45 and 300 hours;

the minimum amount of the extracted residue at 15 hours was delayed a little from the minimal hardness at 12.5 hours. At these times, some precipitates should dissolve into the matrix, followed by reprecipitation within a short time interval. In this study, the amount of the precipitates, MX and  $\text{Cr}_2\text{N}$ , and the chemical composition of MX were calculated on several assumptions; it was found that these values changed discontinuously with the progress of the tempering time (Figure 19). It was also found from Figure 19 that, at the times the amount of  $\text{Cr}_2\text{N}$  showed as minimal, the amount of MX always showed as maximum, and *vice versa*. When the amount of  $\text{Cr}_2\text{N}$  showed as minimal, *i.e.*, when the  $\text{Cr}_2\text{N}$  dissolved into the matrix, the average chemical composition of MX became Cr rich. Conversely, when the amount of  $\text{Cr}_2\text{N}$  increased, *e.g.*, at 100 and 1000 hours in Figure 19, the average chemical composition of MX became V and Nb rich. During the discontinuous changes in the chemical composition of the MX, the average composition of the MX nitride changed from  $(\text{Cr}_{0.65}\text{V}_{0.25}\text{Nb}_{0.1})\text{N}$  to  $(\text{Cr}_{0.35}\text{V}_{0.45}\text{Nb}_{0.2})\text{N}$ , based on the ICP-AES data of Figure 19.

The changes in the composition of the MX and in the amount of the MX and  $\text{Cr}_2\text{N}$  took place at the occurrence of the discontinuous changes in the hardness and preferred orientation. After correlating these changes with each other, the changes near 15 hours could be explained as follows. Subgrains began originating from 10 hours, accompanying the discontinuous changes in the preferred orientation (Figure 3); the subgrains took over the pre-existing lath martensite and particles, such as  $\text{Cr}_2\text{N}$ , precipitated on the pre-existing lath boundaries. At this time, the  $\text{Cr}_2\text{N}$  particles would have dissolved into the matrix, because the amount of  $\text{Cr}_2\text{N}$  decreased at around 15 hours (Figure 19). For the same reason, it would be impossible for the  $\text{Cr}_2\text{N}$  to grow along the boundaries. It is also impossible that the  $\text{Cr}_2\text{N}$  particles left behind from the boundaries grew individually after the formation of new subgrains. We also found an increase in the amount of the MX at this time (15 hours), and the MX particles would have formed on the new precipitation sites, *i.e.*, the new subboundaries, nearby lath boundaries, and pre-existing MX particles. Then, after the discontinuous changes occurred from 10 to 15 hours, the  $\text{Cr}_2\text{N}$  continued to reprecipitate until 40 hours. Although by tempering at 750 °C for around 15 hours, not only the  $\text{Cr}_2\text{N}$  but also the MX particles lying at the lath boundaries should dissolve into the matrix, it was possible to determine only the difference between the decrease and increase in the amount of the MX and the increase in the Cr content of the MX from Figure 19.

After the initiation of a discontinuous change, the opposite reactions, *i.e.*, the dissolution of the  $\text{Cr}_2\text{N}$  and the precipitation of the MX and *vice versa*, were always found. Therefore, the following explanation is possible. The nucleation of subgrains triggered the dissolution of the  $\text{Cr}_2\text{N}$ , which was a nonequibrated reaction. This reaction, therefore, released Cr atoms diffused to the nearby MX particles and changed the average composition of the MX, or formed Cr-rich MX on the new

precipitation sites; this state was also not thermally equilibrated, and finally Cr<sub>2</sub>N began to precipitate again toward an equilibrated state, squeezing Cr atoms from the temporarily formed Cr-rich MX particles. If we recall that the chemical composition of individual MX particles was scattered in a wide range throughout the process of tempering, as shown in Figure 20, it was more feasible for the Cr-rich MX particles to newly form on the boundaries rather than on the pre-existing MX particles. If the released Cr atoms diffused to the pre-existing MX particles and precipitated on them, the chemical composition of the MX would tend to converge to a certain value.

The problem of why the MX instead of the Cr<sub>2</sub>N precipitated after the Cr<sub>2</sub>N dissolved could be explained as follows. It might be possible that, after the Cr<sub>2</sub>N dissolved, Cr-rich MX was first formed and then was gradually replaced by the Cr<sub>2</sub>N. This might be plausible if we could assume that the thermodynamic properties of Cr-rich MX were similar to those of CrN, because the formation free energy of the CrN was nearly same as that of the Cr<sub>2</sub>N; however, the Cr<sub>2</sub>N was slightly more stable as compared to the CrN,<sup>[33]</sup> and the CrN easily nucleated, due to a small coherency strain of CrN, as compared to Cr<sub>2</sub>N. Finally, stable Cr<sub>2</sub>N was formed and the amount of Cr<sub>2</sub>N increased gradually.

Again, the discontinuous change in the preferred orientation would occur, which caused the dissolution of the Cr<sub>2</sub>N. These processes would be repeated until 1000 hours at the occurrence of the discontinuous changes in the preferred orientation, although discontinuous changes were not observed at 100 hours, in the hardness and XRD data.

In the explanation offered here, there was another question as to why the nucleation of the subgrains, which was presumed from the discontinuous changes in the preferred orientation, caused the dissolution of the precipitates (Figure 19). It might be possible that the vacancy concentration at a moment of the formation of subgrains was high enough to dissolve many more atoms than that in the state of lath martensite. However, we have no information to support this idea. Another idea was based on an energy consideration. In the case of boundary precipitation with coherent strain, the local Gibbs free energy change,  $\Delta G_I$ , is expressed by the following equation:

$$\Delta G_I = -\Delta G_f + E_{el} + \gamma - E_{int} \quad [5]$$

where  $\Delta G_f$ ,  $E_{el}$ ,  $\gamma$ , and  $E_{int}$  are the driving force term for precipitation, the elastic energy term due to coherency strain, the interface energy term, and the elastic interaction term between coherent strain and boundary dislocations, respectively, and the boundary dislocation energy term was omitted. After the lath boundary was taken over by a subgrain, the local Gibbs free energy change is denoted by  $\Delta G_{II}$  and

$$\Delta G_{II} - \Delta G_I = E_{int} > 0 \quad [6]$$

Therefore, the state of the precipitates apart from the boundary would be energetically unstable, and then the

precipitate particle might shrink or dissolve into the matrix.

Gustafson and Ågren<sup>[34]</sup> gave a model of carbo-nitride nucleation on a dislocation in a 10 pct Cr steel; they estimated that the interaction energy between a dislocation and coherency strain was approximately the dislocation line energy times the size of a particle. The value of the interaction energy was not so small as to consider it negligible; it depended on the magnitude of the coherency strain. If the precipitates grew large, the coherency might break down. Therefore, the elastic energy term decreased; interfacial dislocations should be generated around the particle however, and, thus, the interaction energy term increased, due to the elastic interaction between the interfacial dislocations and the boundary dislocations. Therefore, the noncoherent particles that precipitated on the boundaries also became unstable; they might dissolve into the matrix if the particle size is small after the disappearance of the precipitation site, *i.e.*, boundaries.

The martensite structure, in general, is continuously recovered by tempering, but the discontinuous changes in the hardness (Figure 2) and the preferred orientation (Figure 3) were thought to be related to the nucleation of the subgrains, based on the EBSD measurements of a similar steel. As shown in Figure 22, the apparent activation energy for the occurrence of the discontinuous hardness change was nearly equal to the activation energy of the lattice diffusion of an interstitial element. Possible reactions corresponding to this apparent activation energy were considered to be the dissolution of the Cr<sub>2</sub>N and the decomposition of the Cr-rich MX particle. The dissolution of the Cr<sub>2</sub>N meant that, accompanying the nucleation of the subgrains, a Cr<sub>2</sub>N particle precipitated on the lath boundary and left alone in the matrix was dissolving into the matrix, as explained previously; in this case, the diffusion of the N atoms controlled the rate of the reaction. The decomposition of the Cr-rich MX particle meant that, just prior to the initiation of the discontinuous hardness change, the amount of the Cr<sub>2</sub>N tended to increase and the Cr content in the MX tended to decrease (Figure 19), which might suggest that the Cr-rich MX particles precipitated on the lath boundaries tended to dissolve and form Cr<sub>2</sub>N, by squeezing N from the Cr-rich MX particle. In this case, the diffusion of N also controlled the rate of the reaction. In any case, it was not easy to explain the relation between these reactions and the changes in hardness at around 12.5 hours in Figure 2. The reason for this might be that the small crest and trough were seen when the discontinuous change at 12.5 hours was enlarged, as shown in Figure 2. Further study is necessary.

When the tempering time was near 45 and 300 hours, similar discontinuous changes in the preferred orientation (Figure 3), the total amount of extracted residue (Figure 6), the amount of MX and Cr<sub>2</sub>N, and the composition of the MX (Figure 19) were confirmed. These changes could be explained through the discussion offered here.

### C. Contribution of Precipitates to Creep Resistance

In this article, the precipitation behavior of carbon-free and nitrogen-bearing 7 pct Cr-0.1 pct Mo-0.063 pct Nb martensitic steel was investigated in detail, but creep tests were not done. However, it is important to estimate the contribution of the  $\text{Cr}_2\text{N}$  and MX particles. Both the  $\text{Cr}_2\text{N}$  and the MX precipitated on the lath martensite and prior austenitic grain boundaries, and seldom precipitated in the grains. On the other hand, the well-known 9Cr-1Mo steel precipitated carbide of a NaCl type, both on the boundaries and in the grains.<sup>[21]</sup> Therefore, it was reasonable to consider that, in the present steel, particles precipitated on boundaries locked the lath boundaries and prevented their migration, which increased creep resistance. The  $\text{M}_{23}\text{C}_6$  in a 9Cr-1Mo steel and the  $\text{Cr}_2\text{N}$  in this steel were relatively large; it might be impossible for  $\text{M}_{23}\text{C}_6$  or  $\text{Cr}_2\text{N}$  to cover sufficiently with the boundaries. On the other hand, the carbo-nitride precipitated in a 9Cr-1Mo steel was usually fine, and the time exponent of the particle size was relatively low, *i.e.*, about 0.1 to 0.2, but the constituent metallic element of the carbo-nitride was mainly Nb and V; the amount of the carbo-nitride was about 0.1 pct<sup>[35]</sup> and not very large, and, therefore, all the boundaries could not be locked by the carbo-nitride particles, which might cause the increase in lath width and thus the decrease in creep resistance. On the other hand, the MX nitride in this steel could dissolve considerable amounts of Cr. The amount of MX was rather large, about 0.3 pct; the size was also rather large, 20 to 60 nm; and the time exponent of the particle size was rather high, *i.e.*, 0.2 to 0.3. Therefore, the precipitated MX could occupy a considerable area of the entire lath boundaries for a long time. The observed growth rate of the MX particles of the experimental steel was correlated with the dissolution and reprecipitation of those particles, which was caused by the discontinuous changes in the preferred orientation. This statement was made based on the observations made by tempering only, not by creep deformation. However, during creep of the similar 9Cr steel, the subgrain formation and the changes in the preferred orientation were also confirmed by EBSD measurements.<sup>[36]</sup> Therefore, precipitation behavior similar to that observed in this study could be anticipated during creep of a carbon-free and nitrogen-bearing high-Cr martensitic steel. As shown in Figure 19, the increase in the amount of  $\text{Cr}_2\text{N}$  caused the decrease in the MX; therefore, prevention of the formation of  $\text{Cr}_2\text{N}$  was thought to be important.

## V. CONCLUSIONS

The precipitation behavior of carbon-free and nitrogen-bearing 7 pct Cr-0.1 pct Mo-0.063 pct Nb martensitic steel during the tempering duration mainly at 750 °C for a maximum of 1000 hours was studied using XRD, TEM, and ICP-AES, and the following conclusions were obtained.

1. The hardness decreased monotonically with the advance of tempering, in general, but discontinuous

changes were observed in an isothermal tempering curve.

2. Synchronized with the discontinuous hardness changes, the XRD intensity, apparent lattice strain, and apparent crystalline grain size, which were calculated from the integral breadth of the diffraction peaks of the matrix, changed discontinuously. These phenomena were thought to be caused by the discontinuous changes in the substructures during the tempering of martensite, *e.g.*, the formation of subgrains.
3. The MX nitride of cubic structure was a major precipitate; the smaller amount of hcp  $\text{Cr}_2\text{N}$  was formed during tempering, but Z phase was not confirmed.
4. The amount of MX tended to gradually decrease with the crest and trough; on the other hand, the  $\text{Cr}_2\text{N}$  increased. During the tempering period at 750 °C for a maximum of 1000 hours, the crest and trough occurred at the times of the discontinuous changes in hardness; the amount of the MX increased when the amount of the  $\text{Cr}_2\text{N}$  decreased and *vice versa*.
5. The MX particles were fine and were rectangular parallelepiped-like, with an aspect ratio of 1.5. The time exponent of the grain size was 0.2 to 0.3. The major constituent metallic elements of the particles were Cr, V, and Nb, and the average chemical composition of the MX changed roughly from  $(\text{Cr}_{0.65}\text{V}_{0.25}\text{Nb}_{0.1})\text{N}$  to  $(\text{Cr}_{0.35}\text{V}_{0.45}\text{Nb}_{0.2})\text{N}$ , although the chemical composition of the MX changed discontinuously at the times when the discontinuous change in hardness occurred. Moreover, the chemical composition was distributed in a wide range around the average value, throughout the tempering period at 750 °C for a maximum of 1000 hours. The XRD peak of the MX could be resolved into three subpeaks, with a different composition for each. The MX particles measured at a lower angle (Nb- or V-rich) were formed at a later stage of tempering and replaced the MX particles measured at a higher angle (Cr-rich). The particle size of the MX measured by XRD seemed to be smaller than that measured by TEM, due to the scattering of the chemical composition; the particle size of the MX measured by TEM was apparently larger than that measured by XRD, due to the shape of the precipitates.
6. The  $\text{Cr}_2\text{N}$  particles were coarse and might be plate-like. According to the shape of the  $\text{Cr}_2\text{N}$  particles and the experimental methods, the particle size was apparently large when measured by TEM and small when measured by XRD; the extent of the difference depended on the Miller index and the tempering conditions.
7. The changes in the amount of MX and the composition, which occurred repeatedly during tempering, were thought to be caused by the following processes. The  $\text{Cr}_2\text{N}$  precipitated on lath boundaries was dissolved into the matrix at the times of the discontinuous changes in the preferred orientation, which might correspond to the nucleation of subgrains; the Cr-rich MX was temporarily formed and, finally, the  $\text{Cr}_2\text{N}$  reprecipitated and replaced the Cr-rich MX.



## ACKNOWLEDGMENTS

The authors gratefully acknowledge Dr. Toshiyasu Nishimura, NKK Co. (JFE Steel), for supplying the experimental steel. The authors are also grateful to Mr. Anoop Kabadwal, a student of the graduate school of the National Defense Academy, for preparing the manuscript.

## REFERENCES

1. R.R. Barr and B. Glen: *High Temperature Properties of Steels*, ISI Publishers, London, 1967, No. 97, pp. 225–26.
2. V.K. Sikka, C.T. Ward, and K.C. Thomas: *Ferritic Steels for High Temperature Applications*, ASM INTERNATIONAL, Materials Park, OH, 1983, pp. 65–84.
3. R.L. Klueh and D.R. Harries: *High-Chromium Ferritic and Martensitic Steels for Nuclear Applications*, ASTM, West Conshohocken, PA, 2001, pp. 1–55.
4. S. Ohta: *Ferritic Heat-Resisting Steels*, Chijin Shokan Co., Ltd., Tokyo, 1998, pp. 218–56.
5. F. Abe, S. Nakazawa, H. Araki, and T. Noda: *Metall. Trans. A*, 1992, vol. 23A, pp. 469–77.
6. F. Abe: *Metall. Mater. Trans. A*, 2003, vol. 34A, pp. 913–25.
7. K. Sawada, K. Kubo, and F. Abe: *Mater. Sci. Technol.*, 2003, vol. 19, pp. 732–38.
8. P.J. Ennis, A. Zielinska-Lipiec, O. Watcher, and A. Czyrska-Filemonowicz: *Acta Mater.*, 1997, vol. 47, pp. 4901–07.
9. K. Spiradek, R. Bauer, and G. Zeiler: *Materials for Advanced Power Engineering*, Kluwer Academic Publishers, The Netherlands, 1994, Part I, pp. 251–62.
10. M. Yoshizawa, M. Igarashi, and T. Nishizawa: *Tetsu-to-Hagané*, 2005, vol. 91, pp. 272–77.
11. R. Jayaram and R.L. Klueh: *Metall. Mater. Trans. A*, 1998, vol. 29A, pp. 1551–58.
12. K. Suzuki, S. Kumai, H. Kushima, K. Kimura, and F. Abe: *Tetsu-to-Hagané*, 2003, vol. 89, pp. 691–98.
13. M. Taneike, F. Abe, and K. Sawada: *Nature*, 2003, vol. 424, pp. 294–96.
14. M. Taneike, K. Sawada, and F. Abe: *Metall. Mater. Trans. A*, 2004, vol. 35A, pp. 1255–62.
15. K. Sawada, M. Taneike, K. Kimura, and F. Abe: *ISIJ Int.*, 2004, vol. 44, pp. 1243–49.
16. M. Tamura, H. Iida, H. Kusuyama, K. Shinozuka, and H. Esaka: *ISIJ Int.*, 2004, vol. 44, pp. 153–61.
17. M. Tamura, H. Kusuyama, K. Shinozuka, and H. Esaka: *ISIJ Int.*, 2007, vol. 47, pp. 317–26.
18. M. Tamura, K. Shinozuka, K. Masamura, K. Ishizawa, and S. Sugimoto: *J. Nucl. Mater.*, 1998, vols. 258–63, pp. 1158–62.
19. K. Shinozuka, M. Tamura, and H. Esaka: *Tetsu-to-Hagané*, 2002, vol. 88, pp. 686–93.
20. M. Tamura, K. Ikeda, H. Esaka, and K. Shinozuka: *ISIJ Int.*, 2001, vol. 41, pp. 908–14.
21. K. Suzuki, S. Kumai, Y. Toda, H. Kushima, and K. Kimura: *ISIJ Int.*, 2003, vol. 43, pp. 1089–94.
22. B. Sundman, B. Jansson, and J.-O. Andersson: *Calphad*, 1985, vol. 9, pp. 153–90.
23. W.H. Hall: *The Proceedings of the Physical Society*, The Physical Society of London, London, UK, 1949, vol. 62, pp. 741–43.
24. F.W. Jones: *Proc. R. Soc. London, Ser. A*, 1938, vol. 166, pp. 16–43.
25. I. Park, K. Asakura, T. Fujita, and J. Watanabe: *Tetsu-to-Hagané*, 1980, vol. 86, pp. 82–91.
26. M. Tamura, Y. Haruguchi, M. Yamashita, Y. Nagaoka, K. Ohinata, K. Ohnishi, E. Itoh, H. Ito, K. Shinozuka, and H. Esaka: *ISIJ Int.*, 2006, vol. 46, pp. 1693–1702.
27. D.H. Jack and K.H. Jack: *JISI*, 1972, vol. 209, pp. 790–92.
28. K. Tokuno, K. Hamada, R. Uemori, T. Takeda, and K. Itoh: *Scripta Metall.*, 1991, vol. 25, pp. 871–76.
29. A. Iseta, H. Teranishi, and F. Masuyama: *Tetsu-to-Hagané*, 1990, vol. 76, pp. 1076–83.
30. M. Tamura, K. Shinozuka, H. Esaka, S. Sugimoto, K. Ishizawa, and K. Masamura: *J. Nucl. Mater.*, 2000, vols. 283–287, pp. 667–71.
31. H. Oikawa: *Tech. Rep. Tohoku Univ.*, 1982, vol. 47, pp. 67–77.
32. K. Hirano: *Tekkou-Binran, ISIJ, Maruzen, Tokyo*, 1981, vol. 1, pp. 343–59.
33. T. Mori, H. Ichinose, and A. Morooka: *Tekkou-Binran, ISIJ, Maruzen, Tokyo*, 1981, vol. 1, pp. 3–17.
34. A. Gustafson and J. Agren: *Acta Mater.*, 1998, vol. 46, pp. 81–90.
35. Y. Kadoya, B.F. Dyson, and M. McLean: *Metall. Mater. Trans. A*, 2002, vol. 33A, pp. 2549–57.
36. M. Tamura, M.M. Nowell, K. Shinozuka, and H. Esaka: *Mater. Trans.*, 2006, vol. 47, pp. 1332–40.